# STEREO–PIV AND HOT–WIRE INVESTIGATIONS ON DELTA WING WITH SHARP AND ROUNDED LEADING EDGE

A. Furman, C. Breitsamter

Technische Universität München (TUM), Lehrstuhl für Aerodynamik (AER)
Boltzmannstrasse 15, 85748 Garching
Germany

## OVERVIEW

Steady and unsteady measurement techniques including stereo particle image velocimetry and hot–wire anemometry are used for vortex flow analysis. Selected results from experimental investigations documenting the low–speed flow environment over a $65^o$ swept delta wing are presented. Results obtained include detailed flowfields of the mean and time–dependent velocity components. The structure of the highly turbulent flow is depicted by the time–averaged, root–mean–square and spectral distributions. Thus, detailed insight in the delta wing vortex structure as well as the breakdown phenomenon is obtained. Peaks in the velocity spectra reveal narrow–band concentration of kinetic turbulent energy at burst flow conditions, reflecting the helical mode instability of the breakdown flow.

## NOMENCLATURE

| | |
|---|---|
| $b$ | wing span |
| $b_l$ | local wing span |
| $c_r$ | root chord |
| $d$ | diameter |
| $f$ | frequency |
| $f_{dom}$ | dominant frequency |
| $f_n$ | lens focal length number |
| $F$ | wing area |
| $k$ | reduced frequency |
| $k_{dom}$ | dominant reduced frequency |
| $l$ | length |
| $l_\mu$ | mean aerodynamic chord |
| $Ma_\infty$ | free stream Mach number |
| $p$ | static pressure |
| $p_\infty$ | free stream static pressure |
| $q$ | dynamic pressure |
| $q_\infty$ | free stream dynamic pressure |
| $Re_{l\mu}$ | Reynolds number based on $l_\mu$ |
| $r_{LE}$ | radius of leading edge |
| $s$ | wing semi span |
| $S_{u'_i}$ | power spectrum of velocity fluctuations |
| $S^N_{u'_i}$ | non–dimensional power spectrum of velocity fluctuations |
| $t$ | time |
| $t_M$ | measurement time |
| $\Delta t$ | pulse delay |
| $T$ | temperature |
| $u$, $v$, $w$ | axial, lateral and vertical velocities |
| $\overline{u_i}$ | mean velocity components |
| $u_{i_{rms}}$ | root mean square velocity components |
| $U_\infty$ | free stream velocity |
| $X_{u'_i}$ | Fourier transformed quantity of velocity fluctuations |
| $x$, $y$, $z$ | body–axis coordinates |
| $\alpha$ | angle of attack |
| $\eta$ | fraction of local semi span, $2y/b_l$ |
| $\Lambda$ | aspect ratio |
| $\varphi$ | leading–edge sweep |
| $\rho$ | density |
| $\zeta$ | fraction of local height, $z/b_l$ |

## 1 INTRODUCTION

The aerodynamic characteristics of delta wings have been investigated intensively over the last five decades[9]. The flow separates at the delta wing highly swept leading–edges already at low angles of attack resulting in the development of two large–scale vortices. Vortex formation starts from the rear part to the apex. The separating shear layer rolls up to form a vortex which is positioned over the wing. This primary vortex is fully developed when vorticity feeding exists over the whole leading–edge. The vortex core is the locus of high axial velocities, low static pressures and increased fluctuations in the subcore area due to the steep gradient in the cross flow components. The leading–edge vortices evoke a substantial increase in the velocities on the wing upper surface. This velocity increase leads to a high suction level, with the local pressure minima indicating the track of the vortex axis on the wing surface. Therefore, leading–edge vortices in a fully developed, stable stage create additional lift and an increase in maximum angle of attack improving significantly maneuver capabilities of high–agility aircraft.

Delta wing research activities often focus on a sharp leading–edge because primary separation is fixed and the leading–edge vortex development is less influenced by Reynolds number effects. A rounded leading–edge complicates the vortex aerodynamics as the position of the separation line varies to a certain extent determined by the pressure gradient and the boundary layer development. Thus, leading–edge radius, angle

of attack and Reynolds number are the main parameters adjusting the onset of vortex evolution as well as position and strength of the primary vortex. For the sharp leading–edge case, the angle of attack is the main parameter only. Considering a chordwise station, there is a strong pressure rise moving from the station of the primary vortex suction peak to the leading–edge. Hence, a severe lateral pressure gradient exists. Therefore, a further separation takes place forming a secondary counter-rotating vortex. The evolution of the secondary vortex depends strongly on the presence of a laminar or turbulent boundary layer[11]. Further, leading–edge vortices are subject to breakdown at high angles of attack. Vortex breakdown is caused by the stagnation of the axial core flow due to the increase of the adverse pressure gradient with increasing angle of attack. Thus, the vortex core expands rapidly accompanied by high velocity fluctuations. The corresponding maxima of fluctuation intensity are located in a limited radial range around the burst vortex core. In addition, the breakdown flow exhibits specific instability mechanisms resulting in narrow–band unsteady aerodynamic forces[1]. The calculation and analysis of such unsteady loads is still a challenging problem which needs the correct representation of the turbulent flowfield features.
In the early 1980s Euler methods had reached a development level that an experimental data base was needed for code validation and assessment, especially in the case of leading–edge vortex flow. Therefore, the International Vortex Flow Experiment (VFE–1) has been established carried out in 1984 - 1986. Force and pressure measurements as well as flowfield studies have peen performed on a 65 swept cropped delta wing in several wind tunnel facilities. Results are documented e.g. in Ref. 5 and 18. It was shown that even for sharp leading–edges with fixed primary separation there is some lack in accuracy because the Euler code results suffers from the missing secondary separation. In the last decade there was great success in the development and application of high fidelity computational fluid dynamics methods. Unsteady Reynolds Averaged Navier–Stokes (URANS) methods are available including a variety of turbulence models based on algebraic up to Reynolds stress transport equations[4,17]. Further, methods for Detached Eddy Simulations (DES) are formulated as a combination of a Large Eddy Simulation (LES) to model separated flow dominated by large–scale structures in the outer domain and a turbulence model to calculate flow quantities in the wall–bounded domain[16]. Even the upper wing surface pressure distribution is very sensitive to correct modeling viscous effects on the wing as well as in the rolled–up shear layers. Therefore, a second International Vortex Flow Experiment (VFE–2) has been proposed to set up an experimental data base for leading–edge vortex flows including both sharp and rounded leading–edge geometry[12]. Latest experimental techniques should be applied to gather the data focusing particularly on turbulence and boundary layer quantities. This integrated research activity including partners from Europe and the United States has been started in 2004 and is still on–going.
The present investigation is conducted in the frame of the VFE–2 consortium. A generic $65^o$ swept delta wing configuration[2,3,6,12] is used to study the complex and relevant flow physics in greater detail than it would be possible for a full aircraft configuration. Both sharp and blunt leading–edge cases are addressed.
Up to now, the experiments include steady and unsteady surface pressure measurements and flow visualization using laser light sheet as well as oil flow technique. Steady pressure measurements served as comparison to reference results obtained by NASA[2,3]. Unsteady pressure measurements inform about vortex bursting when increased pressure fluctuations dominate the breakdown flow. Laser light sheets orientated perpendicular and parallel to the wing surface show the structure and extension of the leading–edge (primary) vortices and to some extent of the secondary vortices. Oil flow visualization is used to study boundary layer development and surface stream lines[7].
This paper focuses on the particle image velocimetry and hot–wire anemometry investigations to complete the informations of the flow characteristic over the delta wing. Particle image velocimetry results show time–averaged velocities without influencing the flow. Hot–wire anemometry informs about time dependent velocities illustrated here in form of root mean square values and power spectral densities of the velocity fluctuations. Investigations are taken especially for three angels of attack, namely for partly developed ($\alpha = 13^o$), fully developed ($\alpha = 18^o$) and burst ($\alpha = 23^o$) leading–edge vortices.

# 2 EXPERIMENTAL PROGRAM

## 2.1 Facility

The measurements have been performed in the large low–speed wind tunnel A of the Institute of Aerodynamics at the Technische Universität München. The test Mach number is $Ma_\infty = 0.07$ and $Ma_\infty = 0.14$ and the Reynolds number based on the mean aerodynamic chord is $Re_{l_\mu} = 1 \cdot 10^6$ and $Re_{l_\mu} = 2 \cdot 10^6$. Angles of attack are varied between $\alpha = 0^o$ and $\alpha = 30^o$. The wind tunnel is of closed–return type with an open test section. The test section is 2.4 $m$ in width, 1.8 $m$ in height and 4.8 $m$ long. The free stream turbulence intensity is less than 0.4%. The uncertainty in the temporal and spatial mean velocity distribution is less than 0.6%. The uncertainty in free stream direction is below $0.2^o$ and static pressure variations are below 0.4%.

## 2.2 Model

A generic delta wing model was designed to study leading–edge vortex flow features comparing the influence of sharp and rounded leading edges. The present model has a root chord length of $c_r = 0.980\ m$, a wing span of $b = 0.914\ m$, a leading edge sweep of $\varphi_{LE} = 65^o$, a wing area of $S = 0.448\ m^2$ and an aspect ratio of $\Lambda = 1.865$, (Tab. 1) and (Fig. 1).

| | | |
|---|---|---|
| root chord | $c_r$ | $0.980\ m$ |
| wing span | $b = 2s$ | $0.914\ m$ |
| wing area | $F$ | $0.448\ m^2$ |
| mean aerodynamic chord | $l_\mu$ | $2/3c_r$ |
| aspect ratio | $\Lambda$ | 1.865 |
| leading edge sweep angle | $\varphi$ | $65^o$ |

Table 1: Model data.

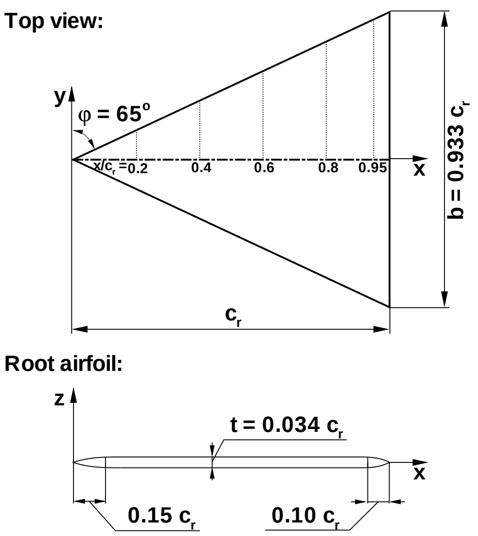


Figure 1: Geometry of the delta wing model.

The delta wing consists of an upper and a lower base

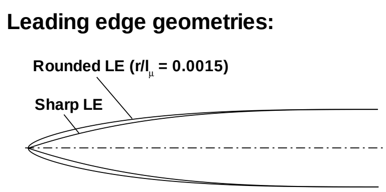


Figure 2: Comparison of leading edge shape.

plate, the trailing edge with a depth of $x_{TE}/c_r = 10\%$ and the pressure orifices being part of these plates. On the inside of these plates cut–outs are milled to house the tubes and wires of the pressure orifices and unsteady pressure transducers, respectively. The thickness of the model is $t = 0.033\ m$, which is constant over the base plate. A sharp and a rounded leading edge ($r_{LE,rounded}/l_\mu = 0.0015$) are available (Fig. 2). The leading edges are fitted on the left and right hand side of the lower base plate and have a depth of $x_{LE}/c_r = 15\%$. Sharp and rounded leading–edge parts are exchangeable. On each of the leading edge elements, five pockets for the pressure sensors have been milled, which are closed with separate lids. A

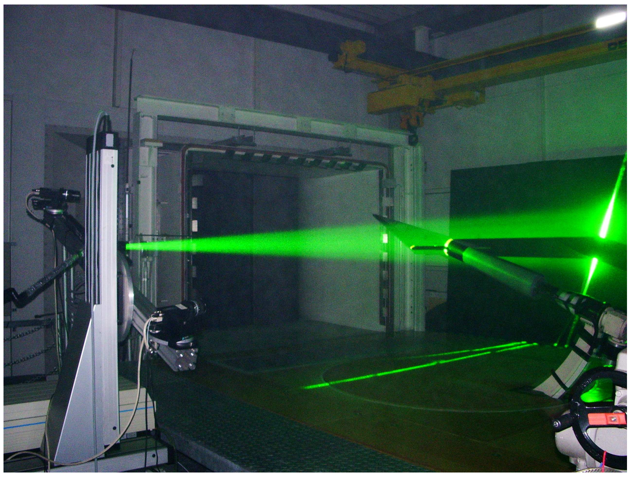

Figure 3: Delta wing model mounted in test section of wind tunnel facility A for PIV application.

model sting is installed on the mounted wing, which is attached to the three–axis model support via a model adapter (Fig. 3). There are 177 pressure orifices with a diameter of $d_d = 0.3\ mm$ situated on the entire wing, of which 44 are equipped with unsteady pressure sensors. The pressure orifices are positioned in five chordwise positions ($x/c_r = 0.2$, 0.4, 0.6, 0.8 and 0.95).

## 2.3 Stereo Particle Image Velocimetry (PIV)

The assembling of Stereo PIV is performed with two cameras left and right of the laser light sheet (Fig. 3). The viewing axes are both around $22^o$ from the light sheet. A pair of 135 $mm$, $f_n = 2.8$ objective lenses constitute the recording optics and are connected to the charge coupled device (CCD) cameras using Scheimpflug–adapters. The adapter afford that the sensor can be correctly and precisely adjusted[15], and therewith the required focusing of the image is achieved with the Scheimpflug angle at $9^o$ for each camera. The cameras are based on a full frame interline transfer CCD sensor with a $1600 \times 1186$ pixel resolution. The field of view covered about 100 $mm$ horizontally and 75 $mm$ vertically. After the calibration and grid generation for $3D$ evaluation the measurements were carried out. The light sheet was generated by a frequency doubled, double oscillator Nd–YAG laser with a power of 200 $mJ$ and a frequency of 10 $Hz$ per pulse. The light sheet thickness was set at approximately 10 $mm$ and the pulse delay was set to $\Delta t = 21\ \mu s$. The measurement validation was accomplished in four steps. First step was the adaptive correlation in interrogation areas of $32 \times 32$ pixels with an overlap of 25%. The second step was the peak validation with a peak height ratio relative to the peak of 1.2. The vector statistics as third step has been carried out with $66 \times 49$ vector values all valid and without substituted vectors of each image. At last the configuration of $3D$ vectors with vector statistics of camera 1 and camera 2 and corresponding calibration grid at oversampling factors 1.0 in $x$ and $y$ direction was performed. The final field of view of the $3D$ image is therefore 460 $mm \times$ 150 $mm$.

### 2.4 Hot–Wire Anemometry (HWA)

For the measurement of fluctuating velocities a dual–sensor hot–wire probe technique is used. The probe consists of two platinum–plated tungsten wires with a diameter of 5 $\mu m$ and a length/diameter ratio of 250 for each wire. The measuring volume formed by the wires is approximately 0.8 $mm$ in diameter and 0.5 $mm$ in height. A sensor angle of $45^o$ is chosen assuming that the best angular resolution will be obtained with pairs of perpendicular wires. The probes were operated by a multi–channel constant–temperature anemometer system. By means of its signal conditioner modules, bridge output voltages were low–pass filtered at 1000 $Hz$ before digitization and amplified for optimal signal level. The sampling time for each channel is 6.4 $s$, with the sampling rate set to 3000 $Hz$, giving a Nyquist frequency of 1500 $Hz$, so that each sample block contains 19200 values. The use of cross–wires generally assumes some knowledge of the flowfield, such as a known flow direction to which the probe must be aligned. The nature of the vortex–dominated flow precludes any knowledge on the direction of the velocity vector everywhere in the field, except for the axial component, which is assumed to be always in the positive $x$–direction. To determine the three velocity components, the probe has to be rotated around its axis by $90^o$ to adjust the wire plane once horizontal and once vertical against the main flow direction. Thus, two triggered traverse sweeps are necessary to obtain the streamwise $u$, lateral $v$ and vertical $w$ components, respectively. Each digitized and temperature corrected voltage pair of the corresponding probe positions was converted to evaluate the time–dependent velocity vector. The numerical method used is based on look–up tables derived from the full velocity and flow angle calibration of the probe[1].

## 3 ANALYSIS OF RESULTS

Three angles of attack were chosen for a detailed analysis, namely $\alpha = 13^o$, $\alpha = 18^o$ and $\alpha = 23^o$. At an angle of attack of $\alpha = 13^o$, the primary vortex is not yet fully developed, at $\alpha = 18^o$ the primary vortex is fully developed, whereas at an angle of attack of $\alpha = 23^o$ the primary vortex breaks down over the wing[8]. Some of the following results are also presented in Ref. 10

### 3.1 Time Averaged Velocity Obtained by Stereo PIV

The time–averaged velocities obtained by Stereo PIV at cross sections $x/c_r = 0.2$, 0.4, 0.6, 0.8 and 0.95 ($Re_{l\mu} = 1 \cdot 10^6$, $Ma = 0.07$) are shown in Figs. 4 and 5. The velocity components in axial direction are displayed as contour plot and in lateral and vertical direction as vector plot. In part a) from each figure the velocity components at angle of attack of $\alpha = 13^o$ are shown, where the primary vortex is not yet fully developed. In that case the biggest difference between sharp and rounded leading edge is visible. At section $x/c_r = 0.2$, the primary vortex structure can be detected for sharp leading edge, but has not reached already the apex. That is perceivable as the axial velocity component decreases after section $x/c_r = 0.4$ ($\overline{u}/U_\infty = 1.58$) to the trailing edge at $x/c_r = 0.95$ ($\overline{u}/U_\infty = 1.21$). In contrast, the rounded leading edge show at section $x/c_r = 0.2$ a transfer from a separation bubble to vortex formation and therewith lower axial velocity level in the vortex core in section $x/c_r = 0.4$ ($\overline{u}/U_\infty = 1.35$). At angle of attack of $\alpha = 18^o$ (figures part b) no significant difference between sharp and rounded leading edge at section $x/c_r = 0.6$ is evident. For both leading edges an axial velocity of $\overline{u}/U_\infty = 1.6$ is observed. At $\alpha = 23^o$, vortex breakdown for the sharp leading edge is slightly further upstream compared to the rounded leading edge. That is also confirmed by the gradient of the axial velocity between chord sections $x/c_r = 0.6$ and $x/c_r = 0.8$, which is $\partial(\overline{u}/U_\infty)/\partial(x/c_r) = -2.450$ for the sharp and $\partial(\overline{u}/U_\infty)/\partial(x/c_r) = -2.245$ for the rounded leading edge. Due to the later separation of the flow on the rounded leading edge, vortex breakdown also occurs later[9,11,13,14] and therewith more kinetic energy is fed into the vortex at this angle of attack. The vortex breakdown is at chord position between $x/c_r = 0.65 \div 0.7$ for the sharp and between $x/c_r = 0.7 \div 0.8$ for the rounded leading edge.

### 3.2 PIV vs. HWA

The comparison between PIV and HWA measurements shows a good agreement between axial, lateral and vertical velocities for sharp (Fig. 6) as well as for rounded (Fig. 7) leading edge. Also, considering the position of the highest velocity peaks for each direction illustrates very good conformity between both measurements techniques.

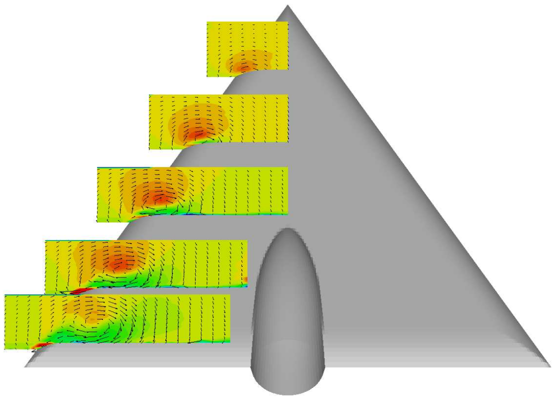

a) Sharp leading edge; $\alpha = 13^o$

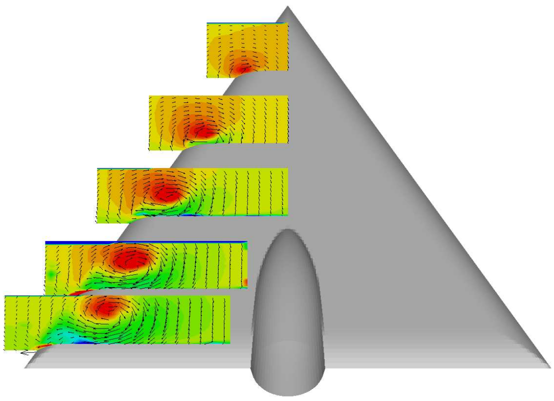

b) Sharp leading edge; $\alpha = 18^o$

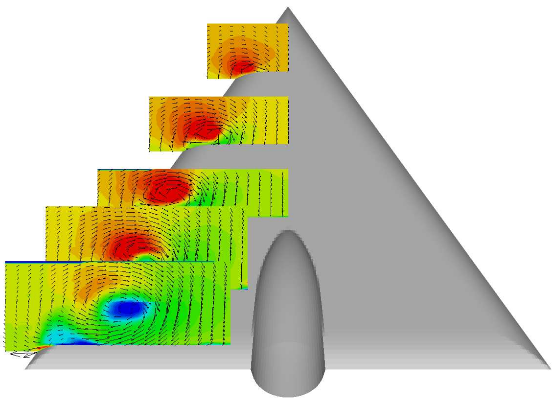

c) Sharp leading edge; $\alpha = 23^o$

Figure 4: Mean velocity distribution at $Re_{l\mu} = 1 \cdot 10^6$ and $Ma = 0.07$ for sharp leading edge.

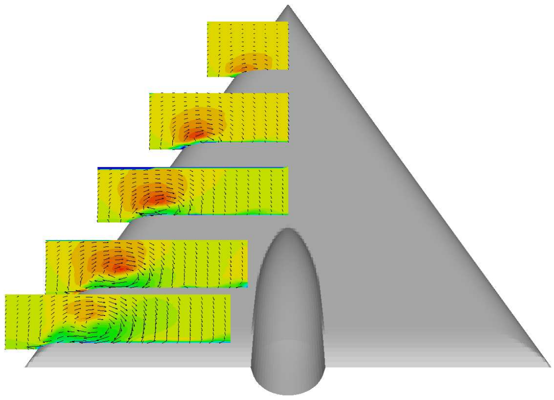

a) Rounded leading edge; $\alpha = 13^o$

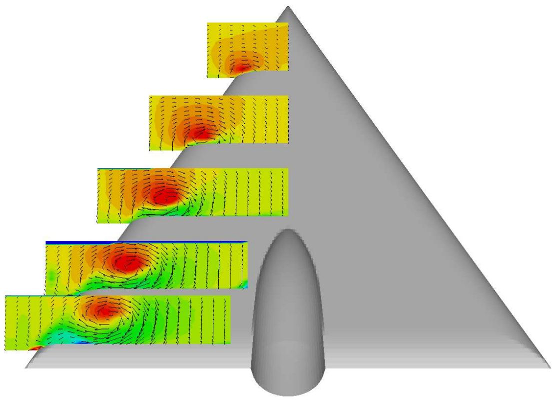

b) Rounded leading edge; $\alpha = 18^o$

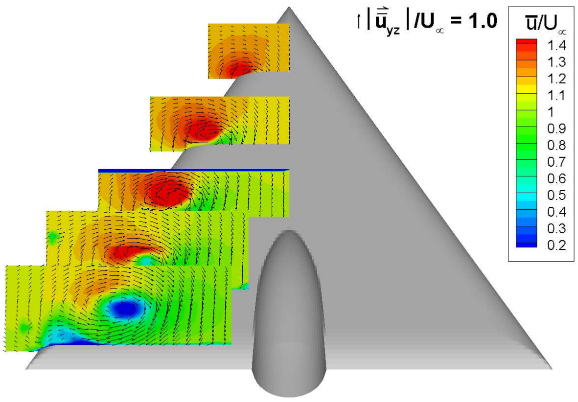


c) Rounded leading edge; $\alpha = 23^o$

Figure 5: Mean velocity distribution at $Re_{l\mu} = 1 \cdot 10^6$ and $Ma = 0.07$ for rounded leading edge.

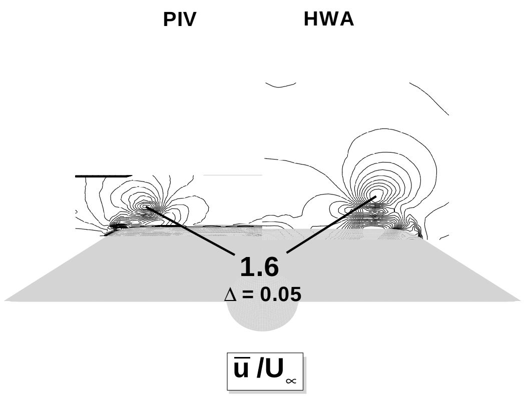


a) Axial velocities.

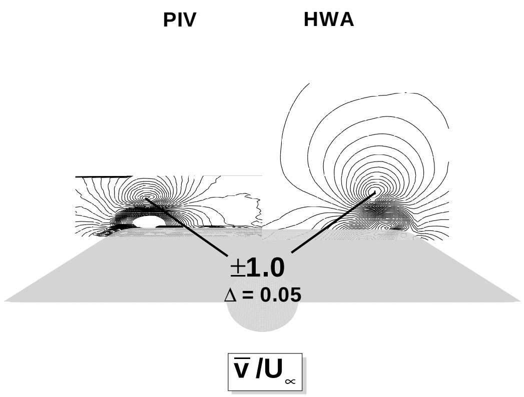


b) Lateral velocities.

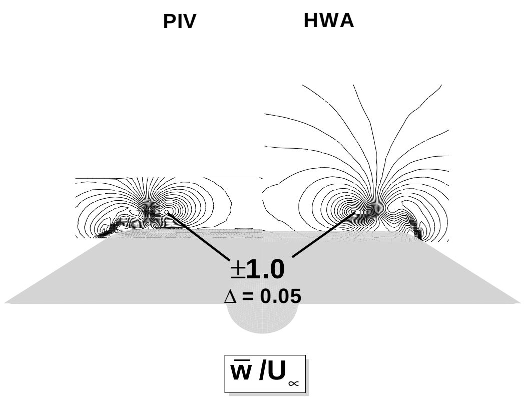


c) Vertical velocities.

Figure 6: Comparison between PIV (left) and HWA results (right) for sharp leading edge at $\alpha = 18^o$, $x/c_r = 0.6$, $Re_{l\mu} = 1 \cdot 10^6$ and $Ma = 0.07$.

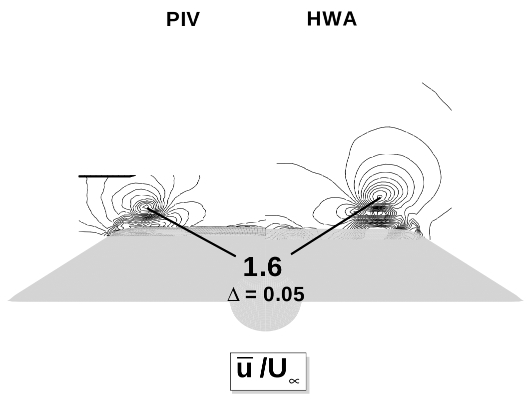


a) Axial velocities.

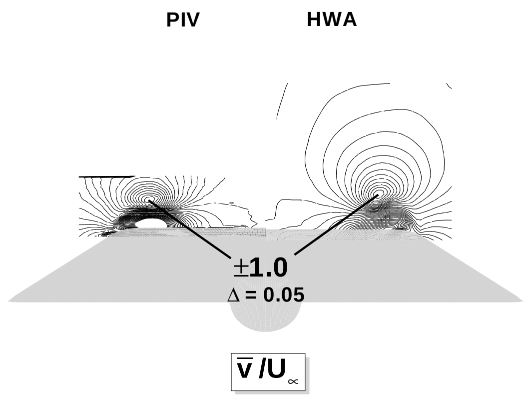


b) Lateral velocities.

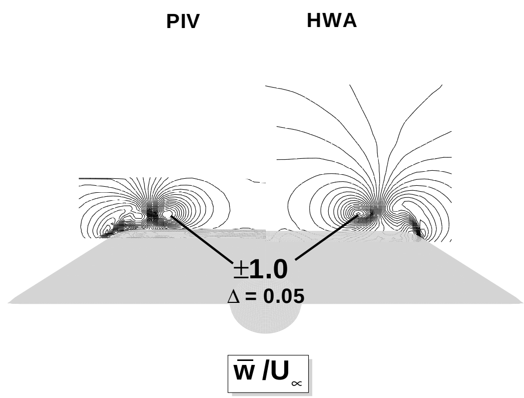


c) Vertical velocities.

Figure 7: Comparison between PIV (left) and HWA results (right) for rounded leading edge at $\alpha = 18^o$, $x/c_r = 0.6$, $Re_{l\mu} = 1 \cdot 10^6$ and $Ma = 0.07$.

### 3.3 Velocity Fluctuation Intensity

For each flowfield position $P$ the time series of the velocities $u_i(P,t)$ are available for every test condition. The average of the velocity $\overline{u}_i(P,t)$ is defined as

$$\overline{u_i}(P) = \frac{1}{t_M} \int_0^{t_M} u_i(P,t)\,dt \quad (1)$$

where $t_M$ is the measurement time or the length of the time series. The fluctuation part of the velocity $u_i'(P,t)$ is described by

$$u_i'(P,t) = u_i(P,t) - \overline{u_i}(P). \quad (2)$$

The mean square value of the velocity fluctuations $\overline{u_i'^2}(P)$ is therefore

$$\overline{u_i'^2}(P) = \frac{1}{t_M} \int_0^{t_M} \left[u_i(P,t) - \overline{u_i}(P)\right]^2\,dt. \quad (3)$$

The root mean square value is denoted rms–value $u_{i_{rms}}(P)$ and is converted in non–dimensional values:

$$\frac{u_{i_{rms}}(P)}{U_\infty} = \frac{\sqrt{\overline{u_i'^2}(P)}}{U_\infty} \quad (4)$$

The intensity of the axial velocity fluctuations shows high values for the separating shear layer, the primary vortex core and the secondary vortex region (Figs. 8 and 9). Peak values are found in the vortex core areas for the fully developed vortex. Downstream, the region of maximum *rms* values becomes enlarged as the vortex extends in radial direction. This expansion is demonstrated by comparing stations $x/c_r = 0.4$ and $x/c_r = 0.6$ for the case of the sharp leading edge (Fig. 8). The rms peak values differ not significantly between these two stations. Further downstream, $x/c_r = 0.8$, the vortex core region shows a change in the rms pattern forming an annular structure of maximum turbulence intensity. This rms pattern is a characteristic feature of the breakdown flowfield indicating that vortex bursting takes place upstream[1]. The limited radial range of local rms maxima corresponds to the points of inflection in the radial profiles of the retarded axial core flow. The strong expansion of the vortex core due to bursting leads to a decrease in axial velocity. Thus, the vortex core flow changes from jet–type to wake–type. As the rapid vortex core expansion continues downstream velocity magnitude as well as gradients and curvature are reduced in the vortex center area the fluctuation level of which becomes diminished. Therefore, the turbulence intensities are the largest in an annular range where high velocity gradients exist due to the neighboured decelerated core flow. The expanded inner vortex core is then the locus of a lower fluctuation level.
In comparison with mean velocity measurements by PIV no vortex breakdown at $\alpha = 18^o$ and $x/c_r = 0.8$ is shown. This means that the flow in the region downstream of $x/c_r = 0.8$, i.e. near the trailing–edge is very sensitive to a little increase in the adverse pressure gradient. A very small object, i.e. a measuring probe can therefore already induce vortex breakdown.
The case of the rounded leading–edge shows a quite similar sequence in the *rms* velocity pattern when progressing from the apex to the trailing-edge (Fig. 9). At $\alpha = 23^o$, the axial turbulence intensity distributions show that vortex bursting occur upstream of $x/c_r = 0.6$ (Figs. 10 and 11). A comparison of the distributions of rms velocities between the cases of sharp leading-edge and rounded leading–edge demonstrates only slight differences. In the inboard area near the wing surface increasing levels of axial velocity fluctuations are visible in all figures which illustrate and confirm the existence of the apex vortex[7].

### 3.4 Spectral Analysis

Spectral analysis is applied to the velocity time series to study the characteristics in the area of the highest velocity fluctuation intensity. The fluctuation part $u_i'(P,t)$ of the discrete time function $u_i(P,t)$ is Fourier transformed based on the relation

$$X_{u_i'}(P,\omega) = \lim_{t_M \to \infty} \int_0^{t_M} u_i'(P,t)\,e^{-i\,\omega\,t}\,dt. \quad (5)$$

The multiplication of the Fourier transformed quantity $X_{u_i'}(P,\omega)$ with its conjugated complex quantity $X^*_{u_i'}(P,\omega)$ leads to the power spectral density function.

$$S_{u_i'}(P,\omega) = \lim_{t_M \to \infty} \frac{2}{t_M}\, X^*_{u_i'}(P,\omega)\, X^T_{u_i'}(P,\omega) \quad (6)$$

The power spectral density of the velocity fluctuations has the dimension of square velocity and time. Taking into account the definition of the reduced frequency (Eq. 8) leads to the non dimensional power spectral density of the velocity fluctuations:

$$S^N_{u_i'}(P,k) = \frac{U_\infty}{l_\mu \overline{u_i'^2}}\, S_{u_i'}(P,k) \quad (7)$$

$$k = \frac{f l_\mu}{U_\infty} \quad (8)$$

The power spectral density distributions of the axial velocity fluctuations are shown for a number of measurement points crossing laterally through the vortex core region and the separating shear layer. The angles of attack discussed include $\alpha = 18^o$ and $23^o$. The measurement stations are depicted in Figs. 12 and 14 for the three cross sections of interest, namely $x/c_r = 0.4$, 0.6 and 0.8, with respect to the contour lines of the

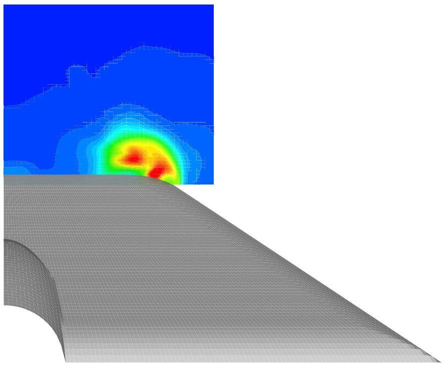

a) $x/c_r = 0.4$

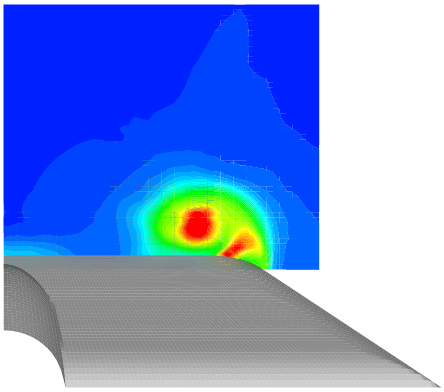

b) $x/c_r = 0.6$

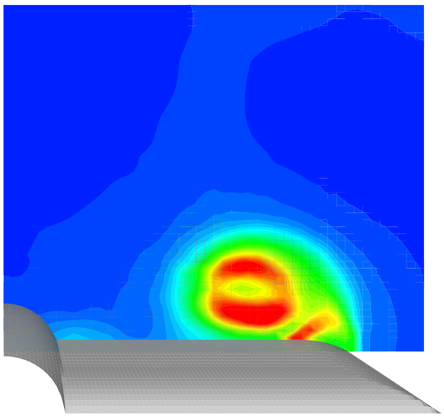

c) $x/c_r = 0.8$

Figure 8: Turbulence intensity distribution of the axial velocity fluctuations for sharp leading edge at $\alpha = 18^o$, $Re_{l\mu} = 1 \cdot 10^6$ and $Ma = 0.07$.

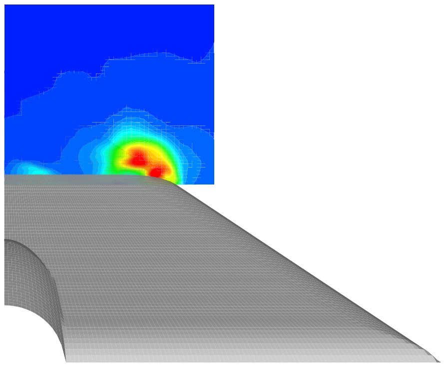

a) $x/c_r = 0.4$

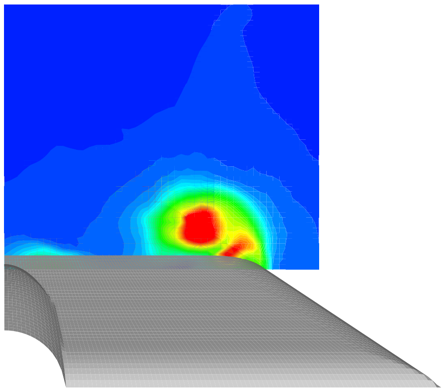

b) $x/c_r = 0.6$

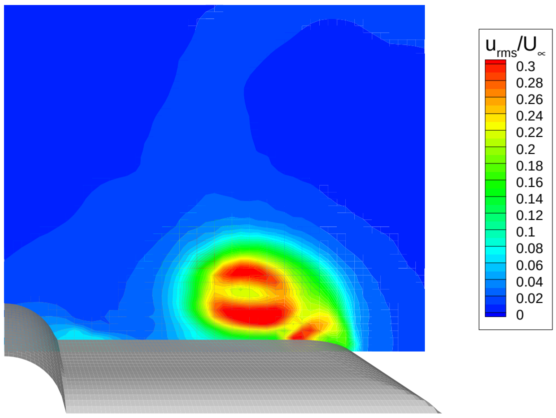


c) $x/c_r = 0.8$

Figure 9: Turbulence intensity distribution of the axial velocity fluctuations for rounded leading edge at $\alpha = 18^o$, $Re_{l\mu} = 1 \cdot 10^6$ and $Ma = 0.07$.

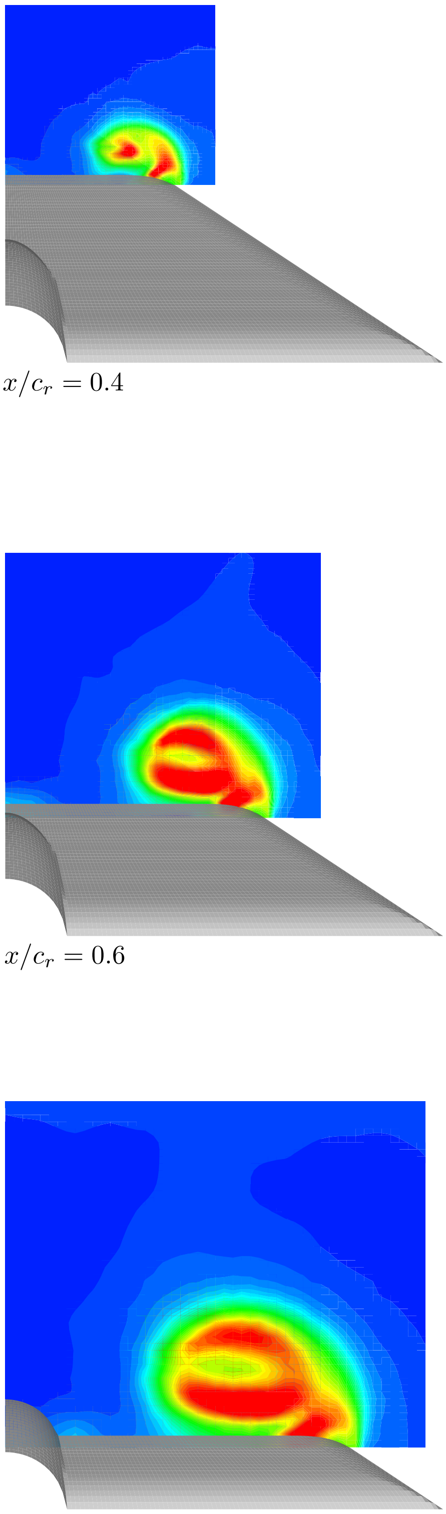

a) $x/c_r = 0.4$

b) $x/c_r = 0.6$

c) $x/c_r = 0.8$

Figure 10: Turbulence intensity distribution of the axial velocity fluctuations for sharp leading edge at $\alpha = 23^o$, $Re_{l\mu} = 1 \cdot 10^6$ and $Ma = 0.07$.

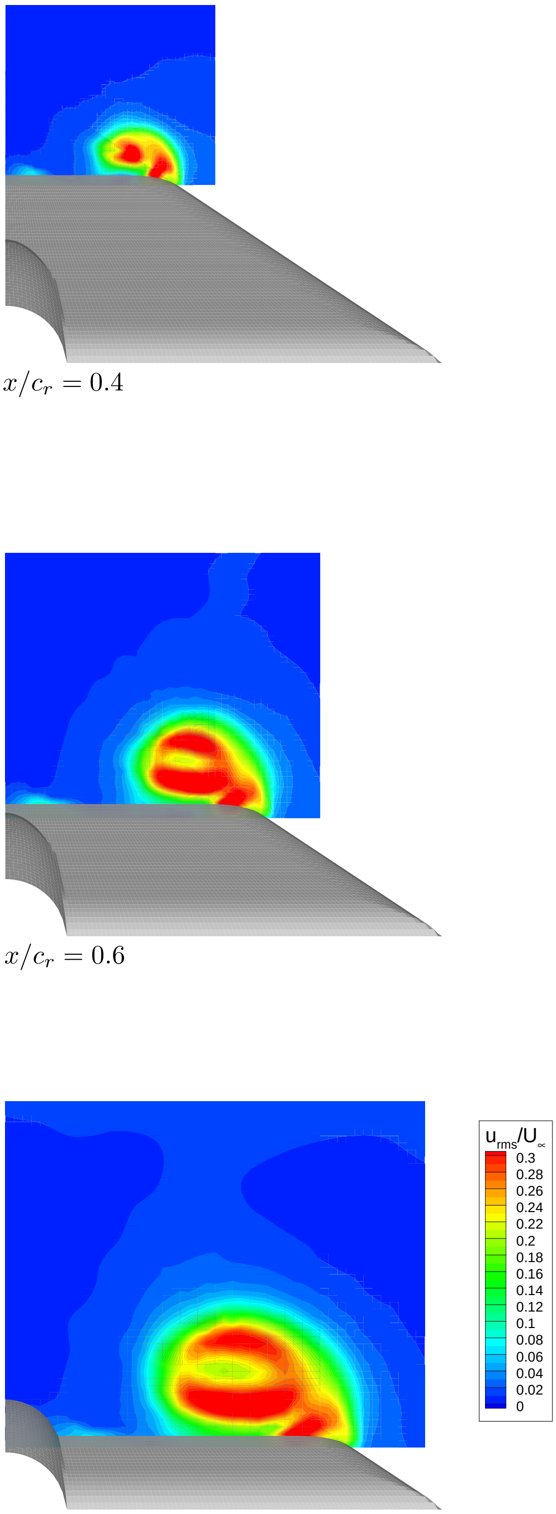


a) $x/c_r = 0.4$

b) $x/c_r = 0.6$

c) $x/c_r = 0.8$

Figure 11: Turbulence intensity distribution of the axial velocity fluctuations for rounded leading edge at $\alpha = 23^o$, $Re_{l\mu} = 1 \cdot 10^6$ and $Ma = 0.07$.

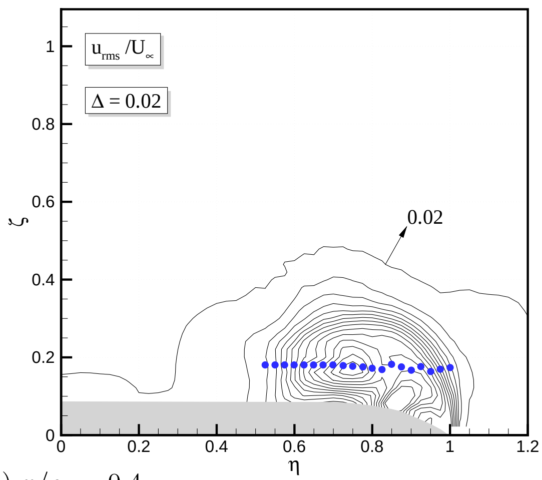


a) $x/c_r = 0.4$

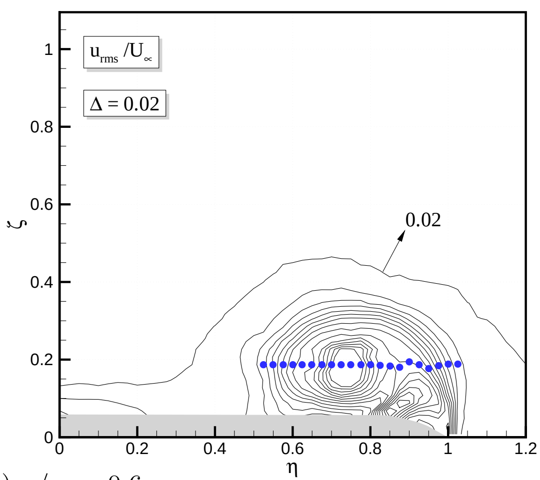


b) $x/c_r = 0.6$

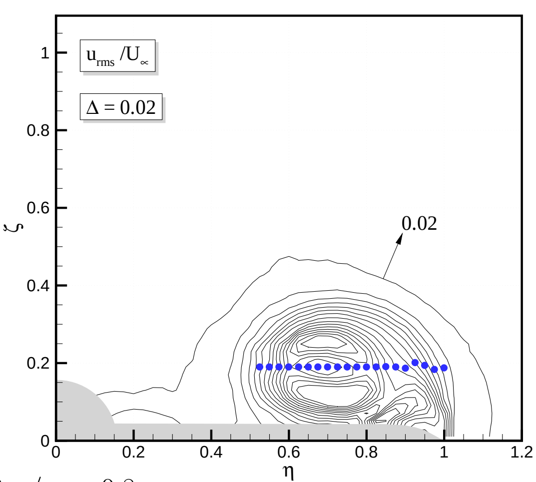


c) $x/c_r = 0.8$

Figure 12: Turbulence intensity distribution of the axial velocity fluctuations for sharp leading edge at $\alpha = 18^o$, $Re_{l\mu} = 1 \cdot 10^6$ and $Ma = 0.07$.

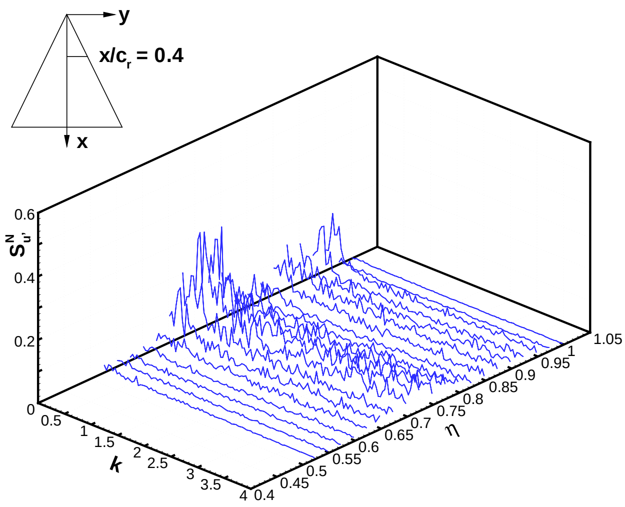


a) $x/c_r = 0.4$

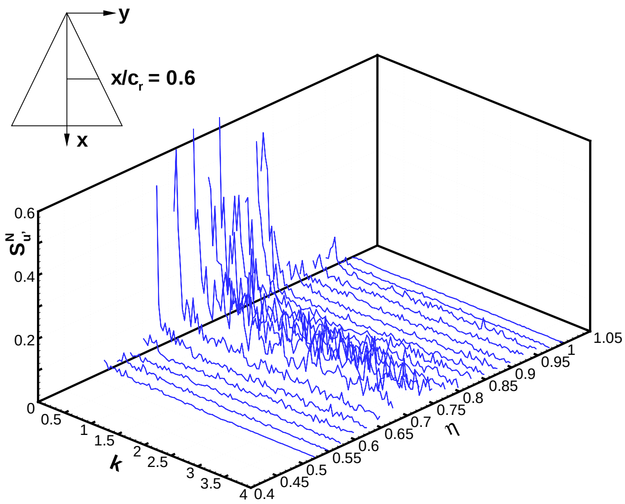


b) $x/c_r = 0.6$

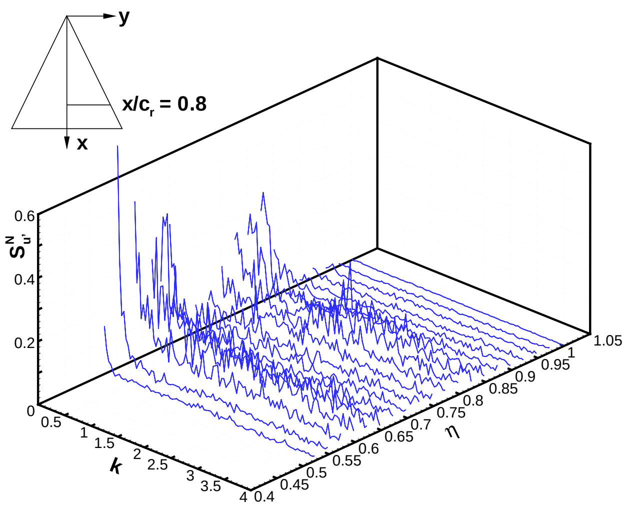


c) $x/c_r = 0.8$

Figure 13: Power spectral density distribution of the axial velocity fluctuations for sharp leading edge at $\alpha = 18^o$, $Re_{l\mu} = 1 \cdot 10^6$ and $Ma = 0.07$.

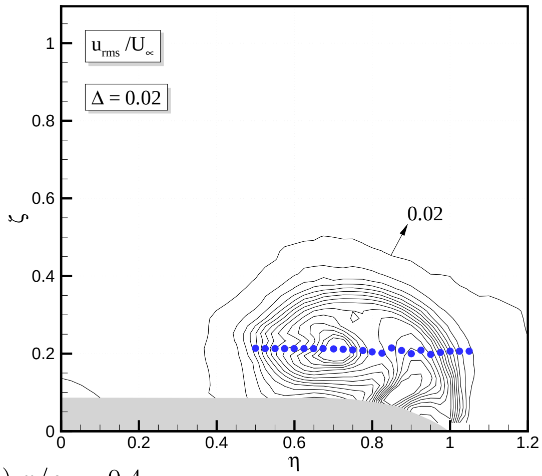


a) $x/c_r = 0.4$

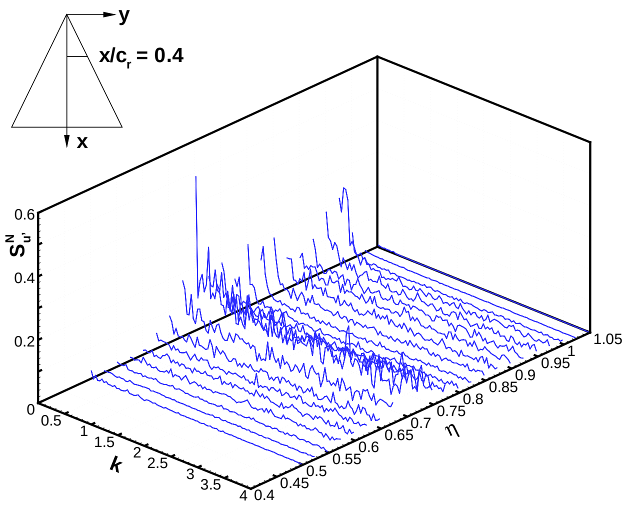


a) $x/c_r = 0.4$

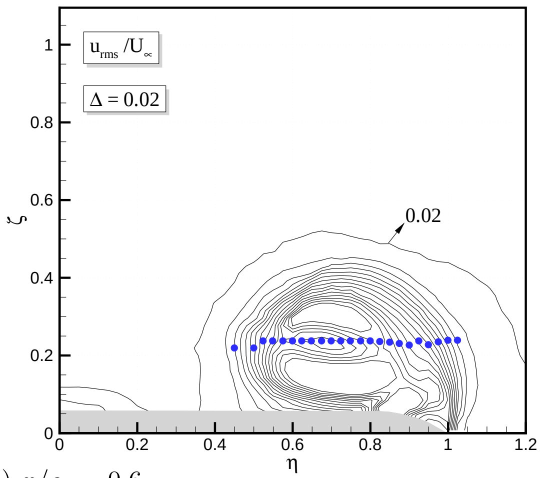


b) $x/c_r = 0.6$

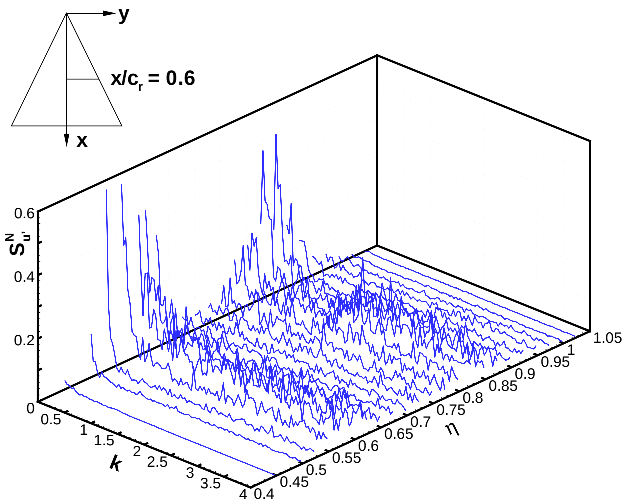


b) $x/c_r = 0.6$

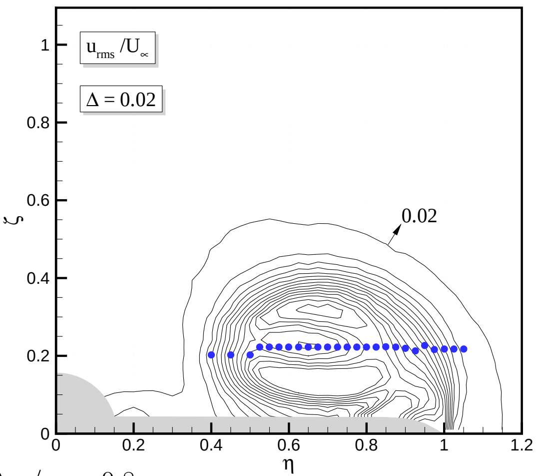


c) $x/c_r = 0.8$

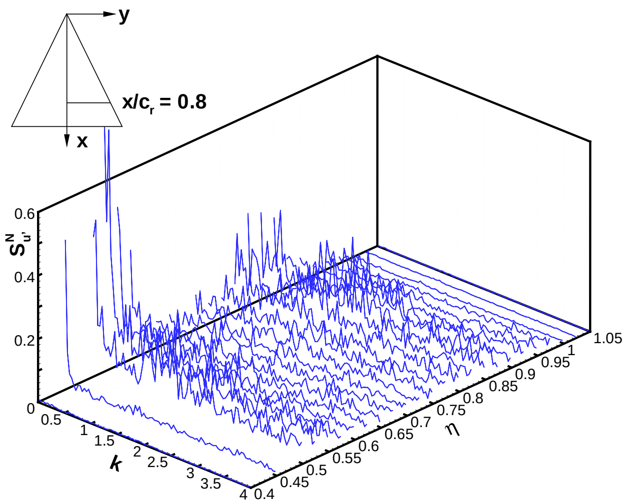


c) $x/c_r = 0.8$

Figure 14: Turbulence intensity distribution of the axial velocity fluctuations for sharp leading edge at $\alpha = 23^o$, $Re_{l\mu} = 1 \cdot 10^6$ and $Ma = 0.07$.

Figure 15: Power spectral density distribution of the axial velocity fluctuations for sharp leading edge at $\alpha = 23^o$, $Re_{l\mu} = 1 \cdot 10^6$ and $Ma = 0.07$.

turbulence intensity distributions of the axial velocity fluctuations. The corresponding power spectral density distributions are plotted in Figs. 13 and 15.
Considering the fully developed leading-edge vortex at $\alpha = 18^o$ and $x/c_r = 0.4$, the power spectral densities exhibit increased values within the vortex core region and the rolled up shear layer (Fig. 13a). Some energy overshoots are present in the low frequency range. At $x/c_r = 0.6$, the power spectral densities of the core region increases revealing again some high peaks at lower frequencies (Fig. 13b). Downstream of vortex breakdown, $x/c_r = 0.8$, the power spectral densities exhibit increased levels in two laterally separated areas matching with the annular structure detected for the turbulence intensity distribution (Fig. 13c). Beside the spectral peaks in the low frequency range there is also a certain increase within a higher frequency range ($k \approx 2 \div 3$) attributed to the helical mode instability of the breakdown flow. This instability results from the wake-type swirling flow in the breakdown region.
The power spectral densities at $\alpha = 23^o$ (Fig. 15) depict again one concentrated area of high fluctuation levels in the vortex core region for the flowfield upstream of vortex breakdown, $x/c_r = 0.4$, and two laterally separated areas of high fluctuation levels downstream of vortex breakdown, $x/c_r = 0.6$. There, an energy concentration can be also observed within $k \approx 2 \div 3$. At $x/c_r = 0.8$ it is found that the concentration of turbulent kinetic energy due to breakdown takes place at lower reduced frequencies, namely within the frequency range of $k \approx 1 \div 2$. As the wavelength of the unstable mode increases with the vortex core expansion and therefore with angle of attack and downstream distance, the associated frequency decreases. This concentration of fluctuating energy within a certain frequency band gives also rise to coherent unsteady pressures creating a frequency dependent loading on the affected lifting surface.

## 4 CONCLUSION AND OUTLOOK

Extensive experimental investigations have been conducted on the low–speed flow environment of a $65^o$ delta wing configuration including sharp and rounded leading edges. Particle image velocimetry provide time–averaged velocities at five chord stations ($x/c_r =$ 0.2, 0.4, 0.6, 0.8 and 0.95) and advanced hot–wire anemometry is used to measure the time–dependent flowfield velocities in cross flow planes located at three stations ($x/c_r = 0.4$, 0.6 and 0.8). The main results of these investigations are addressed for typical vortex topologies at three angels of attack at a Reynolds number based on the mean aerodynamic chord of $Re_{l\mu} = 1 \cdot 10^6$:

- leading edge vortex evolution at $\alpha = 13^o$.
- fully developed leading edge vortex at $\alpha = 18^o$.
- vortex breakdown over the wing at $\alpha = 23^o$.

The comparison between PIV and HWA measurements shows a good agreement for the flowfields of mean velocities. Distributions of axial $rms$ velocities show peak values in the primary vortex core and in the area of the secondary vortex and increased values in the inboard area of the wing on the position of the apex vortex. Downstream of vortex bursting local $rms$ maxima are concentrated on a limited radial range around the expanded inner vortex core. This annular region is also the locus of a concentration of turbulent kinetic energy within a certain frequency band due to a helical mode instability. Hence, this data base provides mean, turbulent and spectral flowfield quantities to be used for comparison with CFD results.
The research work will be continued conducting near–wall measurements based on advanced hot–wire anemometry to obtain information on the three–dimensional boundary layer associated with the formation of the different vortical structures.

**ACKNOWLEDGEMENT**

The support of this investigation by the German Research Association (DFG) is gratefully acknowledged. Furthermore the authors would like to thank the VFE–2 network for the good scientific co–operation.

# References

[1] C. Breitsamter. *Turbulente Strömungsstrukturen an Flugzeugkonfigurationen mit Vorderkantenwirbeln.* Dissertation, Technische Universität München, Herbert Utz Verlag, ISBN 3–89675–201–4, 1997.

[2] J. Chu and J. M. Luckring. *Experimental Surface Pressure Data Obtained on 65° Delta Wing Across Reynolds Number and Mach Number Ranges.* NASA–TM–4645, Volume 1–Sharp Leading Edge, 1996.

[3] J. Chu and J. M. Luckring. *Experimental Surface Pressure Data Obtained on 65° Delta Wing Across Reynolds Number and Mach Number Ranges.* NASA–TM–4645, Volume 3–Medium–Radius Leading Edge, 1996.

[4] S. Crippa and A. Rizzi. Initial Steady/Unsteady CFD Analysis of Vortex Flow Over the VFE–2 Delta Wing. In $25^{th}$ *Congress of the International Council of the Aeronautical Sciences*, ICAS 2006–P2.18, Hamburg, Germany, 3. – 8. September, 2006.

[5] A. Elsenaar, L. Hjelmberg, K. Bütefisch, and W. J. Bannink. The International Vortex Flow Experiment. In *Validation of Computational Fluid Dynamics, AGARD–CP–437, Vol. 1*, pages 9–1 – 9–23, Lisbon, Portugal, May 2-5 1988.

[6] A. Furman and C. Breitsamter. Delta Wing Steady Pressure Investigations for Sharp and Rounded Leading Edges. In *New Results in Numerical and Experimental Fluid Mechanics V*, pages 77–84. 14. DGLR–Fach–Symposium der STAB, Bremen, Germany, 16. – 18. November, 2004.

[7] A. Furman and C. Breitsamter. Investigation of Flow Phenomena on Generic Delta Wing. In $25^{th}$ *Congress of the International Council of the Aeronautical Sciences*, ICAS 2006–3.1.2, Hamburg, Germany, 3. – 8. September, 2006.

[8] I. Gursul. Criteria for Location of Vortex Breakdown over Delta Wings. *Technical note, Aeronautical Journal*, May, 1995.

[9] D. Hummel. On the Vortex Formation Over a Slender Wing at Large Angles of Incidence. In *High Angle of Attack Aerodynamics, AGARD–CP–247*, pages 15–1–15–17, Sandefjord, Norway, Oct. 4-6 1978.

[10] D. Hummel. The Second International Vortex Flow Experiment (VFE–2) Objectives and Present Status. In $25^{th}$ *AIAA Applied Aerodynamics Conference*, AIAA 2007–4446, Miami, Florida, 25. – 28. June, 2007.

[11] D. Hummel. Effects of Boundary Layer Formation on the Vortical Flow above Slender Delta Wing. In *RTO Symposium on Enhancement of NATO Military Flight Vehicle Performance by Management of Interacting Boundary Layer Transition and Separation*, Paper 30, Prague, Czech Republic, 4. – 7. October, 2004.

[12] D. Hummel and G. Redeker. A new Vortex Flow Experiment for Computer Code Validation. In *RTO Symposium on Advanced Flow Management*, Paper 8, Loen, Norway, 7. – 11. Mai, 2001.

[13] J. M. Luckring. Reynolds Number and Leading–Edge Bluntness Effects on a $65^o$ Delta–Wing. In *40th AIAA Aerospace Sciences Meeting & Exhibit*, Reno, Nevada, 14. – 17. January, 2002.

[14] J. M. Luckring. Reynolds Number, Compressibility, and Leading–Edge Bluntness Effects on Delta–Wing Aerodynamics. In $24^{th}$ *Congress of the International Council of the Aeronautical Sciences*, ICAS–2004–4.1.4, Yokohama, Japan, 29. August – 3. September, 2004.

[15] M. Raffel, C. Willert, and J. Kompenhans. *Particle Image Velocimetry–A Practical Guide.* Springer Verlag, ISBN 3–540–63683–8, 1998.

[16] L. A. Schiavetta, K. Badcock, and R. Cummings. Comparison of DES and URANS for Unsteady Vortical Flows Over Delta Wings. AIAA 2007–1085, 2007.

[17] L. A. Schiavetta, O. J. Boelens, and W. Fritz. Analysis of Transonic Flow on a Slender Delta Wing Using CFD. AIAA 2006–3171, 2006.

[18] B. Wagner, S. Hitzel, M. A. Schmatz, W. Schwarz, A. Hilgenstock, and S. Scherr. Status of CFD Validation on the Vortex Flow Experiment. *AGARD–CP–437*, pages 10–1 to 10–10, 1988.